A Network Optimized Ridge Estimator for Robust PSI Parameter Estimation and Its Application on Deformation Monitoring of Urban Area

Wenqing Wu, Jun Hu, *Member, IEEE*, Zhigui Du, Jingxin Hou, Wanji Zheng, and Jihong Liu

***Abstract*—Persistent scatterer (PS) interferometry (PSI) has the ability to achieve submeter-scale digital elevation model and millimeter-scale deformation. However, it is difficult to maintain good performance under long baseline and large phase gradient. In this article, we develop a network optimized ridge estimator for two-tier network PSI. Such a method can increase parameter estimation robustness and spatial continuity in single-prime mode and urban build environments. First, we construct an optimized first-tier network by outlier detection and subsets network construction. On this basis, we utilize the ridge estimator as a substitute for the weighted least squares (WLS) estimator to improve the estimation accuracy in network adjustment. In the second-tier network, we detect the remaining PSs by constructing local star networks, thus increasing the density of the measurements in the first-tier network. The effectiveness of the proposed method is demonstrated by using the 2016–2018 TerraSAR-X dataset acquired in Shenzhen Metropolis, China. In addition, the stress deformation of two typical buildings, i.e., Shenzhen CITIC Building and Shenzhen Convention and Exhibition Center, are monitored and analyzed.**

***Index Terms*—Outlier detection, persistent scatterer interferometry (PSI), ridge estimator, subsets network, two-tier network.**

I. Introduction

THE PERSISTENT scatterer interferometry (PSI), an advanced remote sensing technique, has the ability to stably detect long-term deformation of persistent scatterers (PSs) [1]. With the launch of new generation of spaceborne SAR sensors with very high spatial resolution, e.g., TerraSAR-X/TanDEM-X and COSMO-SkyMed, PSI has new opportunities to serve high-rises, even the single infrastructure [2], [3]. One of the main advantages of PSI is its sensitivity to small deformations. Ferretti *et al.* [4] had shown submillimeter accuracy with an experiment based on dihedral reflectors. With the advent of X-band satellite, PSI has experienced a further improvement, which can sense the thermal displacements that are caused by temperature differences in the imaged area between SAR acquisitions [5], [6]. Furthermore, the single-prime PSI features high sensitivity to the topography and will be propitious to 3-D reconstruction of buildings [7]–[9]. Therefore, the high-resolution single-prime PSI can accurately retrieve the deformation velocity, height, and thermal amplitude in urban areas.

The basic strategy of PSI is to form single-prime interferograms and estimate geophysical parameters (including deformation velocity, topographic residual and thermal expansion) for PSs that are less affected by spatial–temporal decorrelation, even if the spatial–temporal baselines are longer than the critical baseline, which is prone to result in phase decorrelation for the distributed scatterers (DSs) [10]. The low signal-to-noise ratio (SNR) for interferometric phases can disqualify pixels over study area from becoming PS candidates [11]. Consequently, number and distribution of PSs are usually poorly guaranteed. Insufficient PSs could lead to incomplete observations and the loss of details [10]–[12]. To overcome this limitation, the PSI has been evolved to retrieve the deformation from DSs in addition to PSs by exploiting the algorithms such as phase triangulation analysis [10], maximum likelihood estimation [13], eigenvalue decomposition [14], [15], and integer least squares [16]. However, the high computation burden brought by the all interferometric combinations is quite discouraging.

Furthermore, PSI can remove some spatial low-frequency signals such as orbital errors and atmospheric artifacts on an arc-by-arc basis. However, it is unlikely that current PSI methods can completely avoid the effects of these errors. The orbital error permeates every SAR satellite, even TerraSAR-X and Sentinel-1 [17]. Although several methods had been proposed to remove the orbital error in the interferograms, their general drawback is that some displacement signals are removed together with the orbital effects [18]–[21]. Another vital step in PSI is about the treatment of phase ambiguities in the interferometric phases. Some PSI techniques directly retrieve the geophysical components (e.g., deformation velocity and topographic residual) from wrapped phases and then unwrap the residual phase on a sparse grid. To retrieve the signal of interest, various parameter estimators have been developed, such as periodogram [1], [22], integer least squares [30], and least squares with phase ambiguity detector

Manuscript received February 7, 2021; revised March 29, 2021 and April 22, 2021; accepted April 24, 2021. Date of publication April 29, 2021; date of current version June 8, 2021. The work was supported in part by the National Key Basic Research and Development Program of China under Grant 2018YFC1505101, in part by the National Natural Science Foundation of China under Grant 42030112, in part by the Hunan Natural Science Foundation under Grant 2020JJ2043, in part by the Special Fund for the Construction of Innovative Provinces in Hunan under Grant 2019GK5006, and in part by the Project of Innovation-Driven Plan of Central South University under Grant 2019CX007. (*Corresponding author: Jun Hu.*)

Wenqing Wu, Jun Hu, Jingxin Hou, Wanji Zheng, and Jihong Liu are with the School of Geosciences and Info-physics, Central South University, Changsha 410083, China (e-mail: wenqingwu@csu.edu.cn; csuhujun@csu.edu.cn; houjingxin@csu.edu.cn; zhengwanji@csu.edu.cn; liujihong@csu.edu.cn).

Zhigui Du is with the Spacety Company, Ltd, Changsha 410205, China (e-mail: dzhg@spacety.cn).

Digital Object Identifier 10.1109/JSTARS.2021.3076452

[23]. However, the performance of these estimators could be affected by the large surface deformations, strong atmospheric effects, and/or large phase gradients [24]. In the urban build environment, sparse and uneven PSs would generate large phase gradients on the arcs, easily lead to unwrapping error [25], [26].

The two-tier network PSI method is popular in urban areas with abundant artificial buildings [27], [28]. On one hand, this method can deal with PSs and DSs separately to ensure the accuracy of the solution between high-quality observations. On the other hand, it greatly reduces the computational burden of network adjustment since the joint processing of large-area PSs and DSs is inefficient [29], [30]. However, only the largest connected network is utilized in the traditional two-tier network, yielding an irreparable loss of other smaller connected networks which may carry much useful information. To enhance the capability of PSI in urban built environments, we develop a network optimized ridge estimator (abbreviated as NORM) for increasing parameter estimation robustness and spatial continuity. Three specially steps, including outlier detection, subsets network construction and ridge estimate, are integrated into the traditional two-tier network method. The outlier detection is employed to detect and remove the low-quality arcs, and the subsets network will be constructed to increase spatial coverage. On this basis, we utilize the ridge estimator as a substitute for the weighted least squares (WLS) estimator in order to improve the estimation accuracy of the network readjustment [27]. Two examples of Shenzhen CITIC Building and Shenzhen Convention and Exhibition Center have been presented, which demonstrate that the proposed method has great potential in stress deformation monitoring of the buildings.

The rest of the article is organized as follows. In Section II, we review the principles of PSI and the method for two-tier network linking. In Section III, we present the primary procedures of the proposed method. Section IV presents and analyzes the experimental results in Shen Zhen, China. In Section V, we discuss the monitoring results of different two-tier networks and two landmark buildings of Shen Zhen, and a brief conclusion is drawn in Section VI.

II. Principles of Permanent Scatterer Interferometry

A. Phase Modeling and Parameter Estimation

We consider a collection of N SAR images acquired at time instants t_n, $n = 0, \ldots, N-1$. PSI would select the pixels dominated by PSs, and assume that a PS should have the amplitude or phase stability in all images. The wrapped interferometric phase Φ^i is primarily composed of four contributions [1]

$$\Phi^i = \Phi^i_{\text{def}} + \Phi^i_{\text{topo}} + \Phi^i_{\text{APS}} + \Phi^i_{\text{noise}} \tag{1}$$

Where i is the interferogram number, Φ^i_{def} is the deformation phase contribution, Φ^i_{topo} is the topographic phase contribution, Φ^i_{APS} is the atmospheric phase screen (APS) phase contribution, and Φ^i_{noise} is the decorrelation noise phase contribution. For each given arc e, the above equation can be expressed by the model [5], [6]

$$W\left\{\Delta\varphi^{i,e}\right\} = W\left\{\frac{4\pi}{\lambda}\Delta T_i \Delta v^e + \frac{4\pi}{\lambda}\Delta\text{Temp}_i \Delta k^e + \frac{4\pi}{\lambda R \sin\theta} B_i^{\perp} \Delta\varepsilon^e + \Delta\varphi^{i,e}_{\text{res}}\right\} \tag{2}$$

where $W\{\bullet\}$ is the wrapping operator, $\Delta\varphi^{i,e}$ is the unwrapped differential interferometric phase, λ represents the radar wavelength, R represents the slant range, θ depicts incidence angle of satellite, $\Delta T_i, \Delta\text{Temp}_i, B_i^{\perp}$ are the temporal baseline, the temperature baseline, and the spatial perpendicular baseline with respect to the prime image, respectively, Δv^e is the linear deformation velocity, Δk^e represents the thermal amplitude, $\Delta\varepsilon^e$ is the topographic residual, and $\Delta\varphi^{i,e}_{\text{res}}$ is the residual phase component contributed by residual APS and decorrelation noise.

The retrieval of the interferometric phase ambiguity for both DEM generation and surface deformation mapping is usually a challenging problem for multitemporal InSAR techniques. PSI has integrated spatial–temporal unwrapping in wrapped arc phases through parameter estimation and network adjustment. In temporal unwrapping category, the ensemble coherence γ is popular in the community. First, we estimate the relative parameters at the arcs of the reference network by using the periodogram. We can predefine a discrete interval in the searching space to find a solution, which corresponds to the maximum temporal coherence. If the ensemble coherence is less than a given threshold (typically 0.7–0.9), the corresponding arc will be abandoned, thus generating a reference network consisting of so-called high-quality arcs. Before spatial unwrapping, it is necessary to remove isolated subsets and pseudo-PSs. After identifying the largest connected network, the relative parameters of the PSs are integrated from those of the arcs by using network adjustment and reference point, thus generating linear deformation velocity, topographic residual, and thermal map in the whole area. The integration problem is shown as follows:

$$BX = L \tag{3}$$

with

$$\hat{X} = (B^T P B)^{-1} B^T P L \tag{4}$$

where B is the coefficient matrix consisting of -1, 0, and 1; X contains the absolute parameters of PSs; L represents the relative parameters at the arcs; and P is the weight matrix which has a diagonal form and can be determined by the ensemble coherence.

B. Method for Two-Tier Network Linking

How to construct an optimal reference network to connect PSs in arc-based PSI method is also an intractable problem. It is well known that suitable network redundancy is helpful for improving the estimation accuracy and controlling the computation burden. In addition, short arcs would help to remove the atmospheric artifact and reduce the phase gradient in the steep topography areas with stratified APS, but easily resulting in discontinuous network. In consideration of the robustness of

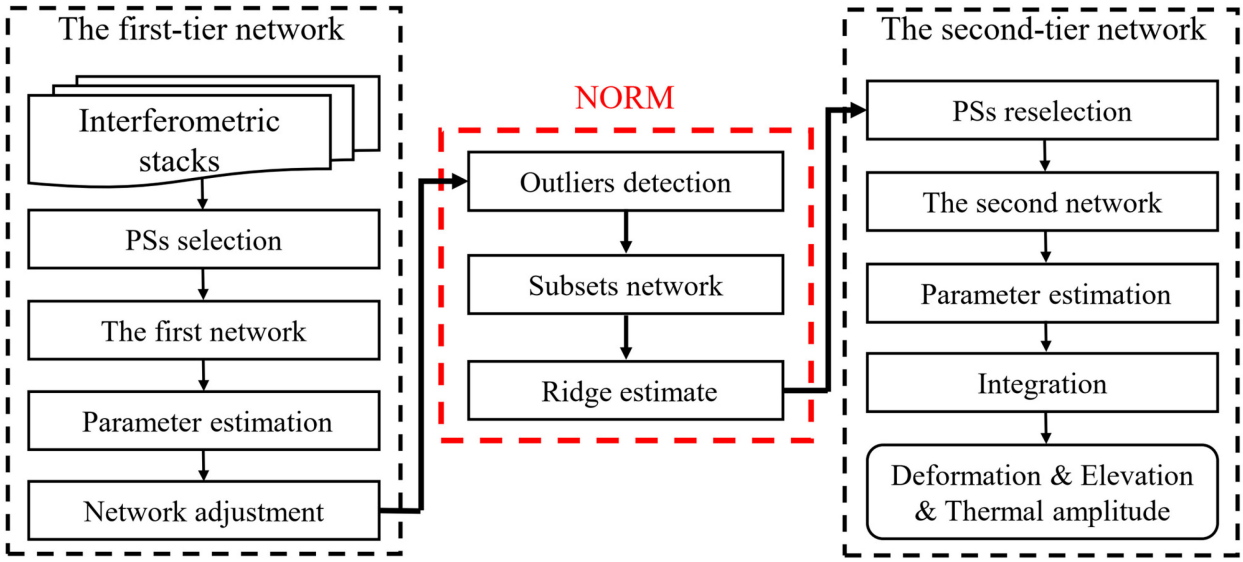

Fig. 1. Flowchart of the two-tier network PSI improved by the NORM algorithm.

parameter estimation, APS correction and computational efficiency, a two-tier network linking method can be used for urban monitoring [27], [28], i.e., Delaunay triangulation network and local star networks.

In the first-tier network, a strict standard (usually amplitude dispersion) is first employed for the selection of primary PS candidates (PPSCs) with high amplitude stability and high SNR. Then, a Delaunay triangulation network will be constructed to connect the PPSCs, and a distance threshold is used to reject the long arcs. When the arc is of short distance, there is high probability that the two adjacent PPSCs have similar APS distribution. Thus, it is easy to calibrate the APS by differencing the phases between the point pair. We then perform the parameter estimation and the network adjustment to identify the largest connected network from the first-tier network. In this article, the largest connected network is treated as the primary first-tier network, which will experience a further optimization. In the second-tier network, the remaining PS candidates (RPSCs) will be detected by using temporally averaged amplitude or coherence. The interferometric quality of the RPSCs is poor guaranteed with a lax standard, and the threshold of ensemble coherence would reject a large number of arcs. We connect each RPSC to the nearest known PS detected in the first-tier network, which forms multiple local star networks. The estimated parameters are relative to the reference PSs from the first-tier network, and thus, we can integrate the parameters of the reference PSs directly to generate the absolute values for the RPSCs. Significantly, the parameter estimation in the second-tier network depends on the quality of the estimation in the first-tier network, self-evidently the first-tier network is important.

III. Methodology Chain of Norm

In this section, a novel two-tier network is introduced for increasing the parameter estimation robustness and space continuity in PSI. Three specially steps will be integrated into the traditional two-tier network method, including outlier detection, subsets network construction, and ridge estimate. The outlier detection is employed to detect and remove the low-quality arcs, and then the subsets network will be constructed to increase the spatial coverage. Afterward, the ridge estimator is exploited as a substitute for the WLS estimator in the network adjustment. A flowchart of the proposed method is shown in Fig. 1.

A. Outlier detection

Before detecting outliers, an initial phase unwrapping has been performed in the primary first-tier network, including periodogram and WLS estimation. The WLS estimator is suitable for the best linear unbiased estimate under random errors. However, during the initial LS estimation, all arcs, including those with phase decorrelation in some interferograms, are used as observations, which will hinder an accurate retrieval of unknowns by direct adjustment. Arc measurements that are contaminated by overwhelming outliers or gross errors should be discarded [23], [25], [26]. The low-quality arcs can be detected by the residual estimates [31]. For each arc, the absolute parameters of PSs can be obtained by (4), and the residual becomes

$$\delta_{\text{res}} = L - B\hat{X}. \tag{5}$$

If the residual is large, it is likely that the absolute estimates on the PSs are unreliable and the corresponding arc should be discarded. The unusual arc measurements are attributed to not only the low-quality interferometric phase but also the estimated error due to large phase gradients in the steep topography areas. To robustly estimate the absolute values of the PSs that are unaffected by outliers or residual distributions, the less or even zero weight should be assigned to those measurements with large residuals. This might bring many isolated subsets and PSs. Alternatively, we are capable of removing the arc measurements

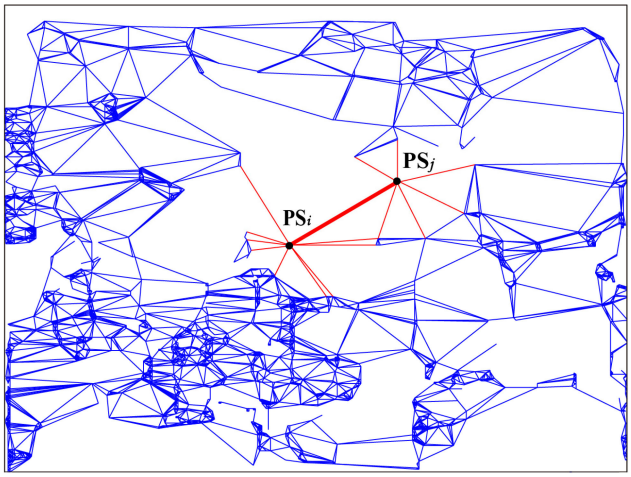

Fig. 2. Blue arcs form the primary first-tier network, the red arcs will be used to detect outliers.

with large residuals to obtain a new largest connected network

$$\max_{\Omega}\{|\delta_{\text{res}}|\} > T_{\delta_{\text{res}}}. \tag{6}$$

For each arc, the set Ω represents the arcs that are connected to the start PS_i and the end PS_j, i.e., the red arcs as shown in Fig. 2. Since the arcs in Ω are closely related in space network, the absolute estimates of PS_i and PS_j should be inaccurate if any arc (including target arc) retains a large residual. Then, it is likely that the target arc is an outlier. However, a large number of arcs will be removed, if the residual threshold $T_{\delta_{\text{res}}}$ is improperly selected. The threshold can be chosen as 3 or 4 for arcs with equal weight, which is considered as an outlier at 95% confidence level [23].

B. Subsets Network Construction

Deleting the arc measurements with large residuals may cause disconnected subsets and PSs. In addition, many isolated subsets have been removed from the initial Delaunay triangulation network, thereby reducing the spatial coverage of the network. If we are interested in the areas covered by these subsets, it is necessary to construct additional networks for them on the basis of the primary first-tier network, and thus combining the subsets and the primary first-tier network to build an optimized first-tier network.

These subsets vary in size and even contain only one PS. The reconstruction of the network for all subsets is time-consuming, the subsets with PSs less than 10 will be abandoned. We first connect all points in each subset to the nearest k points in the primary first-tier network, which will generate a large number of newly added arcs. Similarly, we retrieve the relative parameters of the newly added arcs and select high-quality arcs by ensemble coherence. A higher threshold γ (e.g., 0.8) can be selected to ensure the reliability of these arcs. If at least two points with arcs remaining (to ensure the triangulation), the corresponding subset is then connected to the primary first-tier network by the newly added arcs, otherwise, it will be abandoned [26].

The employment of the nearest neighbor method to construct the subsets network will generate a lot of linearly related arcs, which are approximately parallel in space, resulting in a possible ill-conditioned normal equation matrix $(B^T PB)$. Moreover, the subsets with big size or large quantity will bring a large number of new arc measurements, and then put heavy burdens on network adjustment. Therefore, after selecting the high-quality arcs by ensemble coherence, we removed the arcs with similar slopes. It is well known that two points are capable of forming a straight line with an angle of inclination ranging from 0° to 180°, and this angle of the vector line will be between 0° and 360°. For a subset, we divide 360° into 12 equal parts. The slope of the arcs within each part is considered as similar and only the arc with the largest ensemble coherence is retained. We may also divide the 360° into eighths, sixteenths, and so on for different subsets. This allows efficient connection of subsets and provides a robust reference network for network adjustment.

C. Ridge Estimator

An optimized first-tier network can be obtained by outlier detection and subsets network construction. Based on this network, the WLS estimator shows a better performance in the retrieval of the absolute parameters of the PSs, which is an iterative process of networking and adjusting (see Fig. 1). In practice, however, the sparse matrix B may be ill-conditioned, and the poor condition will result in an unstable inversion. It means that small changes in the observations can cause arbitrarily large changes in the solution. This could be worse in the prosperous urban areas. Therefore, attempting to retrieve parameters directly with the WLS estimator will inevitably generate the solution vector contaminated by noise. Under such circumstances, the ridge estimator is suitable for performing network adjustment instead of the WLS estimator [27]

$$\hat{X} = (B^T PB + \sigma I)^{-1} B^T PL \tag{7}$$

where σ is the regulation parameter and I is an identity matrix. The regulation parameter will be introduced into the WLS estimator to adjust the condition of the coefficient matrix, thus reducing the ill-condition of the normal equation matrix. The effect of regulation varies with different regulation parameters. A suitable parameter can filter out enough noise without losing too much information in the computed solution. Several methods are available for the determination of its value, e.g., L-curve method [32]. The corner of the L-curve corresponds to a good balance between minimization of the solution $\|X\|_2$ and corresponding residual $\|BX - L\|_2$.

IV. Experimental Results and Analysis

A. Study Area and Used Data

Shenzhen, located in the south-central area of Guangdong Province, is the first special economic zone in China. With the rapid growth in population and economy in Shenzhen, geological disasters also occur frequently, thereby bringing tremendous damages to human life and surface architecture. Especially, the uneven deformation has a great impact on the safety of high-rise

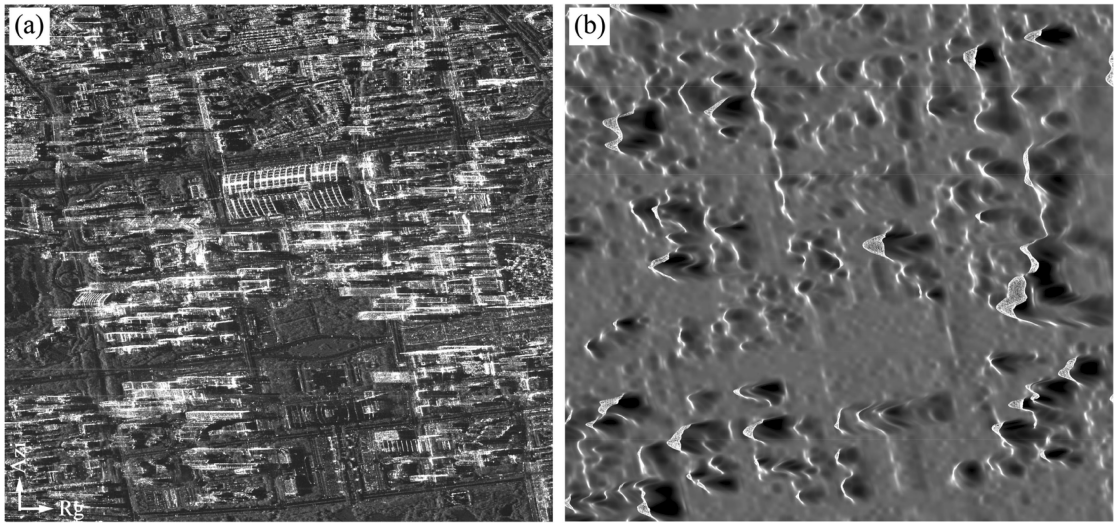

Fig. 3. (a) SAR intensity image. (b) Corresponding AW3D of the study area.

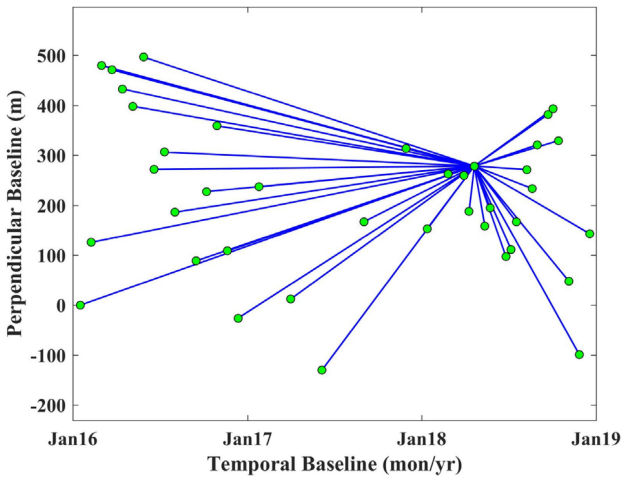

Fig. 4. Temporal and perpendicular baselines of the SAR images.

buildings [33]. The Futian District of Shenzhen is a large central business district led by the Shenzhen Convention and Exhibition Center, where several high-rise office buildings are gathered and serve as the main population centers (see Fig. 3).

A dataset of the ascending TerraSAR-X images (39 scenes) acquired between January 2016 and December 2018 will be employed to monitor the Futian District. Observation parameters for all the images are as follows: incidence angle, 37°; range pixel spacing, 0.9 m; azimuth pixel spacing, 2.0 m; polarization mode, VV. Fig. 4 is the temporal and perpendicular baseline distributions of the interferometric pairs with single-prime, which has a maximum perpendicular baseline of 408 m, and a maximum temporal interval of 825 days. Meanwhile, the AW3D (ALOS (Advanced Land Observing Satellite) World 3D 30 m Resolution DSM) is used to remove the topographic phases. AW3D has a much higher accuracy in urban than those of the ASTER DEM and SRTM DEM, which helps to capture topographic variation and improve geocoding accuracy [34].

B. Test performance in the First-Tier Network

In the first-tier network, we attempt to detect the PPSCs in the study area. The reliable PPSCs would be used as reference points for the second-tier network. First, the calibration of the SAR amplitudes is performed, and the amplitude dispersion (0.6) is then employed for the selection of the PPSCs, as shown in Fig. 5(a). The amplitude and phase instability caused by long baselines can disqualify pixels over study area from becoming PS candidates. There are only 79 066 pixels selected as PPSCs, most of which belong to buildings and highways. These architectures usually have stable reinforced concrete structure and high reflectivity. In contrast, there are few PPSCs selected in the natural surface since the high vegetation coverage in the study area. To estimate geophysical parameters for the PPSCs, we constructed a Delaunay triangulation network, as shown in Fig. 5(b). The area with dense PPSCs can build enough arcs, resulting in a robust local network.

After the initial network construction, we should reject arcs longer than 500 m from the Delaunay triangulation network. The APS will be removed by subtracting the phase of the start PPSC, we then apply periodogram to identify the ensemble coherence and retrieve relative parameters at the arcs. We have predefined three discrete intervals in different search spaces for three parameters. This operation is relatively time-consuming, and its computational efficiency depends on the number of arcs, sampling intervals, and search ranges. The threshold of the ensemble coherence (0.7) is employed to remove low-quality arcs and pseudo-PSs, thereby generating a set of true PSs, which is treated as ideal references for the second-tier network. Before network adjustment, it is necessary to remove isolated subsets and pseudo-PSs, and thus identifying the primary first-tier network. The blue arcs in Fig. 6(a) represent this network, including 200 423 arcs and 74 591 PSs, and approximately 5% of the PPSCs were removed. The primary first-tier network omits other smaller isolated subsets in the first-tier network carry much useful architecture information of the observed scene. It

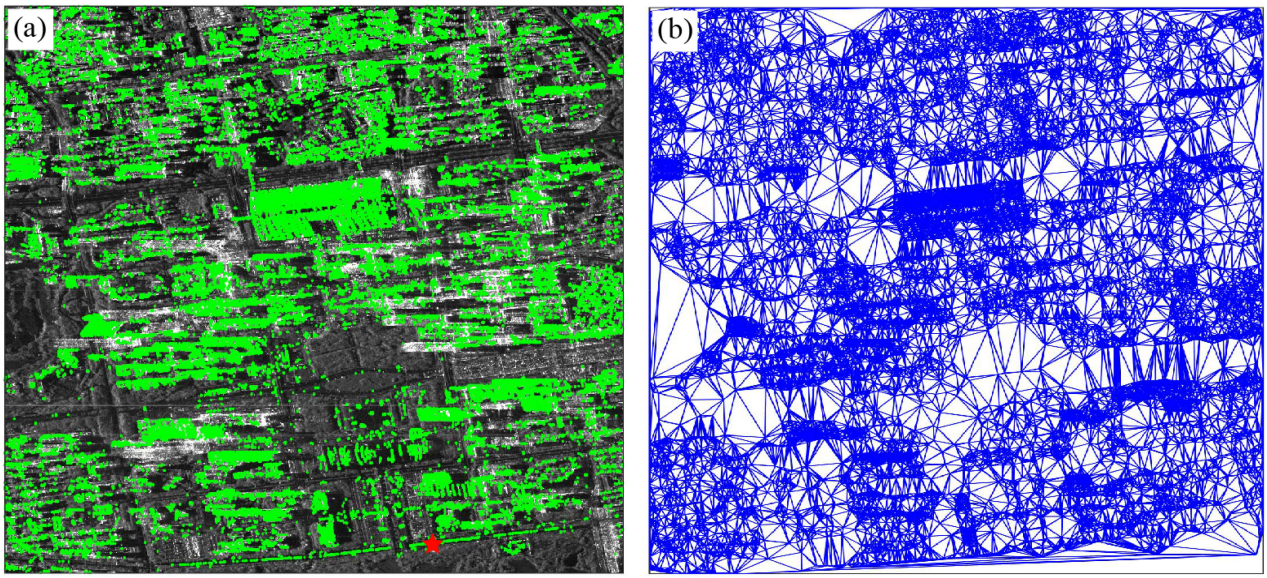

Fig. 5. (a) PPSCs selected in the first-tier network, the red pentagram represents the reference point. (b)Delaunay triangulation network.

is insufficient to merely utilize the primary first-tier network, since its spatial coverage is incomplete when a large number of subsets occur [see the red circles in Fig. 6(a)–(c)].

In the primary first-tier network, we integrate the arc measurements through WLS estimator to retrieve three absolute parameters (deformation velocity, height, and thermal amplitude) of PSs [see Fig. 7(a)–(c)]. Fig. 7(a) is the deformation velocity map in line-of-sight (LOS) direction, ranging from –8 to 8 mm/year; Fig. 7(b) shows the height values of study area, with a range of 0–230 m; The thermal amplitudes [see Fig. 7(c)], increasing with the height of building, are mainly between 0 and 3 mm/°C. The facades of the buildings show obvious thermal effects. Modern high-rise buildings are mainly composed of glass curtainwalls and reinforced concrete, therefore their thermal expansion coefficients increase with the temperatures. At the top of the building, strong solar radiation usually brings high temperature, resulting in large thermal amplitude. In addition, the large-area building features a wide power receiver panel, easily leading to thermal displacements, as shown by the Shenzhen Convention and Exhibition Center in red rectangle A.

However, the outliers have contaminated the deformation velocity [see Fig. 7(a)]. Long baselines are prone to result in phase decoherence, thus generating low-quality phase observations. In addition, small errors in the observations can cause arbitrarily large changes in the solution when the coefficient matrix B is ill-conditioned, which means that the estimate is biased and unreliable. The SAR images acquired from December 2016 to September 2017 have large revisit intervals and spatial baselines with the prime image in our experiment, these low-quality interferometric phases reduce the precision of estimates. Consequently, we construct an optimized first-tier network by outlier detection [see Fig. 6(b)] and subsets network construction [see Fig. 6(d)–(f)]. The empirical threshold $T_{\delta_{\text{res}}}$ is set to be 3, and we define 50 for the number of nearest neighbor k (for computational reasons). Fig. 6(c) is the optimized first-tier network, where 192 302 arcs and 72 206 PSs are preserved. The deformation velocity, height, and thermal amplitude of the PSs can be re-estimated using the WLS estimator in the optimized first-tier network, as shown in Fig. 7(d)–(f). Compared with the estimates in Fig. 7(a)–(c), there are obvious improvements for the deformation velocity in the contaminated areas (especially the areas outlined by the rectangles A and B). Second, the added subsets have improved the spatial continuity of three estimates (e.g., the areas outlined the rectangle C).

The experimental results show that the deformation velocity has a higher sensitivity to the outliers than the height and thermal amplitude, thereby bringing a qualitative improvement to this parameter by the optimized first-tier network. For an intuitive expression, we present the histograms of the velocity estimated in Fig. 7(a) and (d) (see Fig. 8). The histogram of velocity estimates in the primary first-tier network is biased, whereas this bias is effectively rectified by the optimized first-tier network. Since there are outliers occur in observations, we infer that a more robust estimate of deformation velocity can be derived in the optimized first-tier network. In addition, an excellent example to compare the two results is the Shenzhen CITIC Building in red rectangle B. Fig. 9 represents the differences of deformation velocity, height, and thermal amplitude of the Shenzhen CITIC Building between the estimations from the primary and the optimized first-tier networks, which shows that the proposed network has the ability to retrieve more accurate details. Up to 2 mm/year and 5 m can be found in the differences of deformation velocity and height, respectively. The estimated thermal amplitude has differences of 0.1 and –0.1 mm/°C on the left and right of the building, respectively.

The WLS estimator is suitable for the best linear unbiased estimate under Gaussian noise [35]. When the orbital ramps and unwrapping errors occur in the arc measurements, the ill-conditioned coefficient matrix in the WLS estimator will cause unstable solutions. As shown in Fig. 7(d), there are obvious errors (bottom left) in the deformation velocity estimated by using the WLS estimator on the optimized first-tier network.

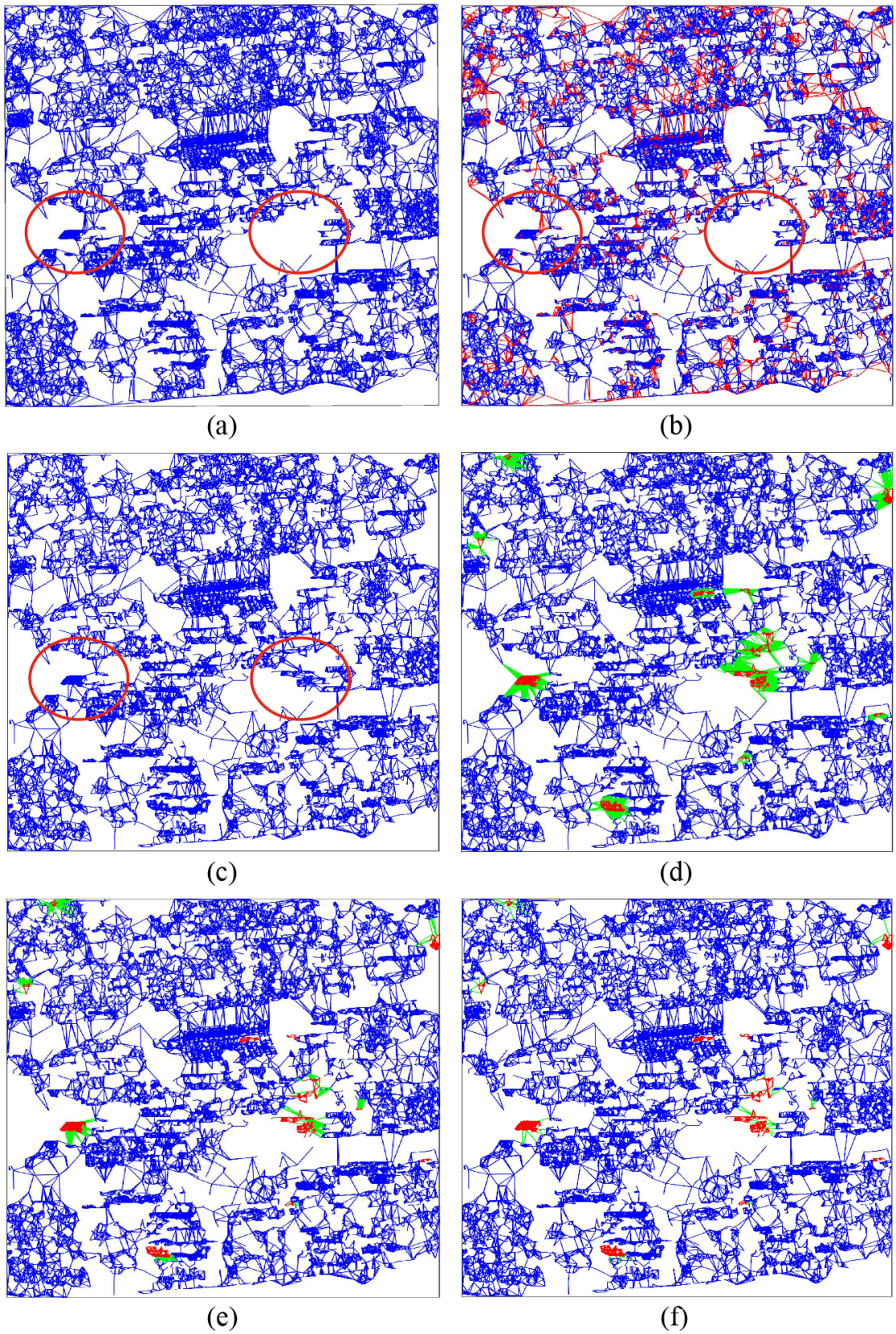

Fig. 6. Establishing the optimized first-tier network by outlier detection and subsets network construction. (a) Primary first-tier network. (b) Red arcs represent the outliers detected in the primary first-tier network. (c) Optimized first-tier network. (d)–(f) show the processes of subsets network construction, the constructed network by (d) the nearest neighbor, (e) the ensemble coherence, and (f) the slope. Blue arcs are derived by removing outliers from the primary first-tier network. The red arcs represent the subsets. The green arcs indicate the newly added arcs.

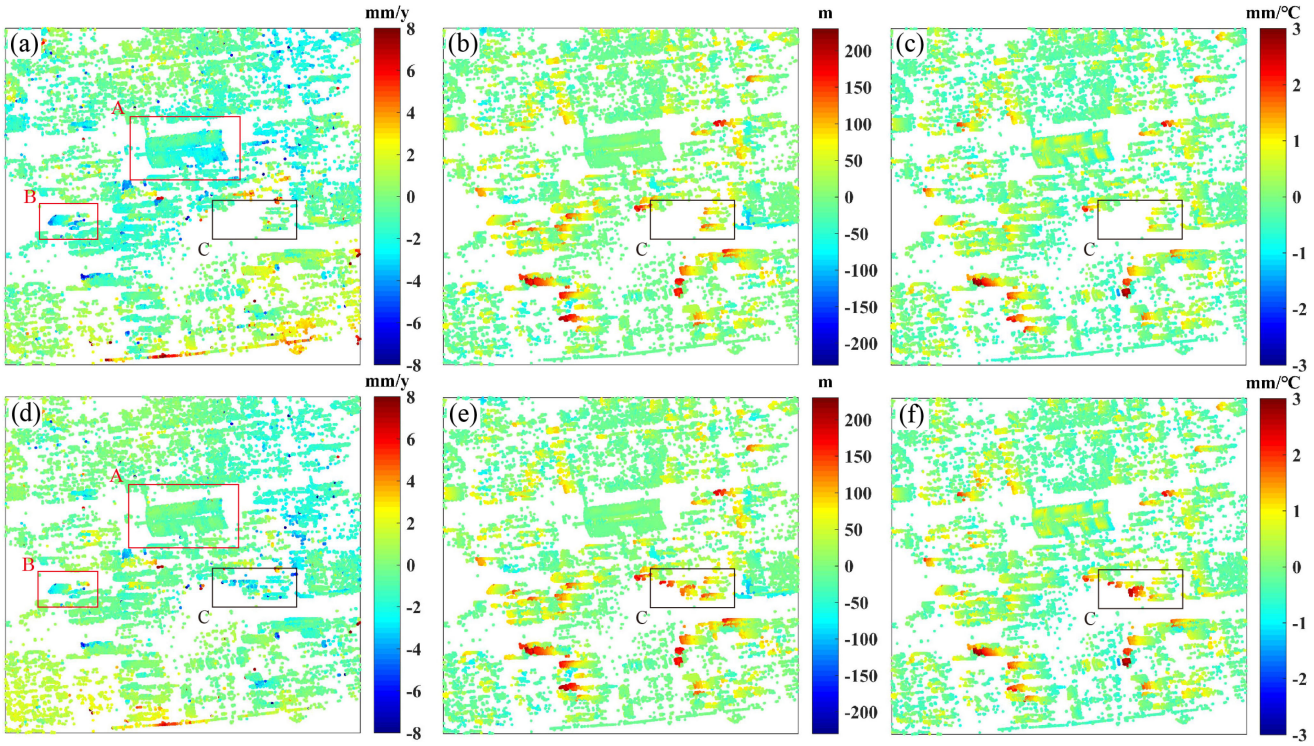

Fig. 7. First line: (a) Deformation velocity, (b) height, and (c) thermal amplitude estimated by the primary first-tier network. Second line: corresponding parameters estimated by the optimized first-tier network.

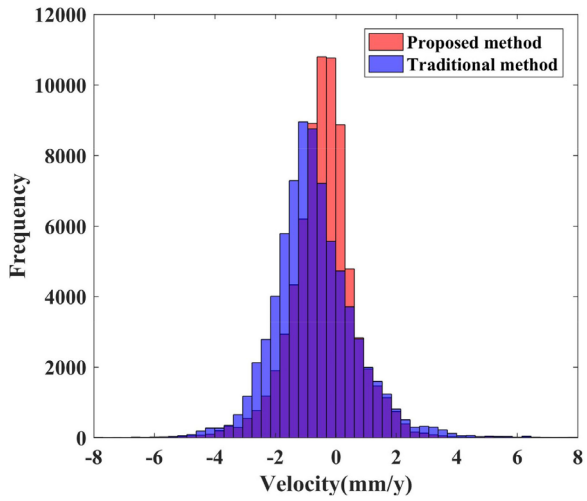

Fig. 8. Histogram of deformation velocity by the primary first-tier network (blue) and the optimized first-tier network (red).

Therefore, the ridge estimator will be employed to integrate arc parameters, and thus generating a global optimal solution. It should be noted that the ridge estimator is a compressive biased estimate, which will lose some useful information for a global optimization. In order to assess the performances of the two estimators, a set of experiments are conducted based on simulated datasets in the Appendix. Considering that the network adjustment for deformation velocity is less stable and has a high sensitivity to errors, the ridge estimator is only utilized to regulate the deformation velocity. By locating the corner of the L-curve, we found the optimal regulation parameter to be 3e-5 for deformation velocity. Fig. 10(a) and (b) present the estimations by using the WLS-estimator and the ridge estimator, and their difference for deformation velocity ranges from –1 to 1 mm/year [see Fig. 10(c)]. The improved estimations confirm that the ridge estimator is helpful for minimizing the global errors, which is popular for small deformation monitoring in urban areas.

C. Test Performance in the Second-Tier Network

In the second-tier network, we detect the remaining PSs to increase the spatial density of measurements. We first selected RPSCs with a temporally averaged coherence larger than 0.5 to distinguish architecture from vegetation, and then removed the PSs detected in the first-tier network. As shown in Fig. 11(a), there are 619 078 pixels selected as RPSCs, covering a large proportion of the buildings and roads. After selecting the RPSCs, we connected each RPSC to the nearest PS detected in the first-tier network and constructed the local star networks [see Fig. 11(b)], including 552 510 arcs. Similarly, we removed the APS by differencing the phase of the point pair for the RPSCs, and the arcs longer than 500 m will be rejected here. Owing to a lax selection criterion, some candidates may be inclined to distributed scatterers [11], we would eliminate a large number of low-quality arcs using ensemble coherence (0.7) to ensure good production. There are 166 902 PSs preserved, approximately 73% of the pseudo-PSs and DSs were removed.

Fig. 12(a)–(c) represent the estimations of the first-tier network. The three absolute parameters (deformation velocity, height, and thermal amplitude) of the PSs can be estimated

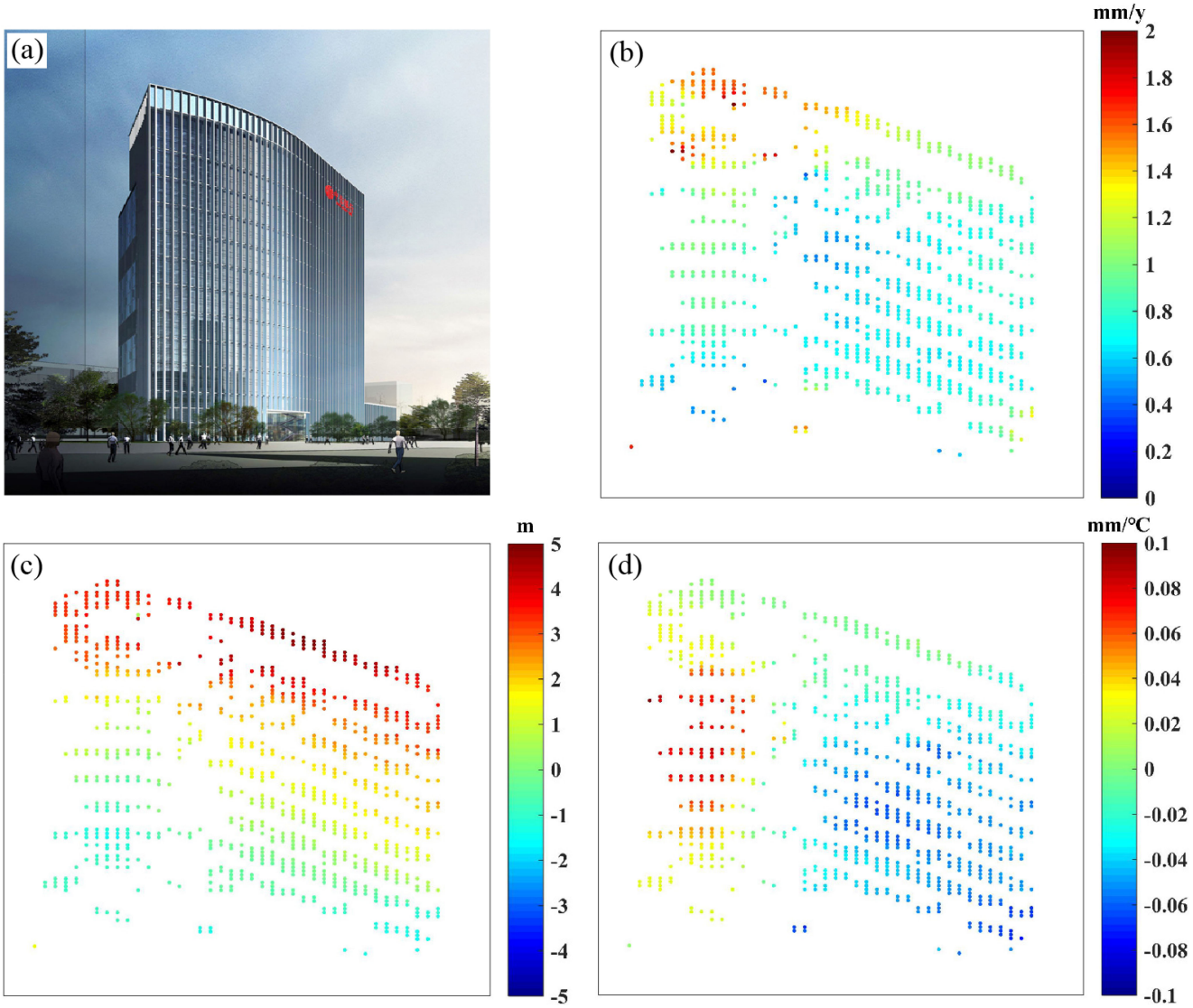

Fig. 9. (a) Picture of Shenzhen CITIC Building. Differences of (b) deformation velocity, (c) height, and (d) thermal amplitude between estimates by the primary first-tier network and the optimized first-tier network.

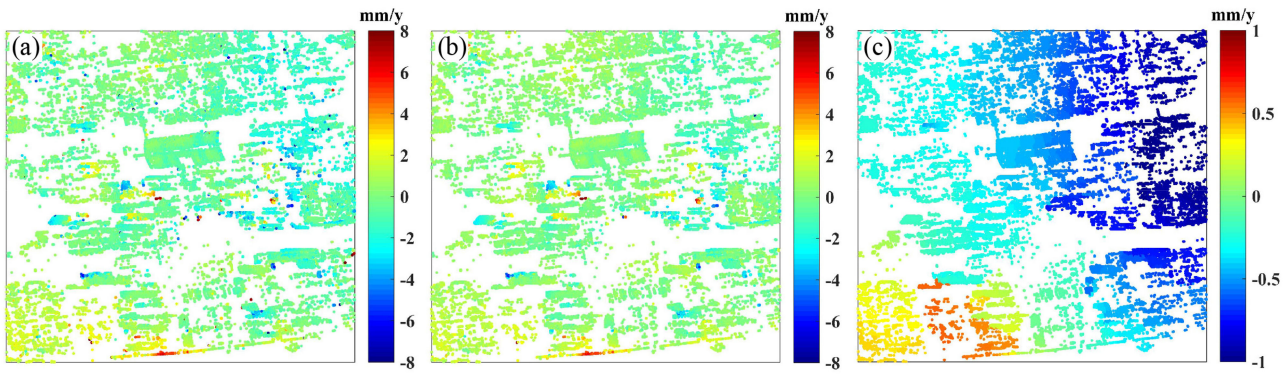

Fig. 10. Deformation velocity estimated by (a) the WLS-estimator and (b) the ridge estimator. (c) Difference between estimates by the WLS-estimator and the ridge estimator.

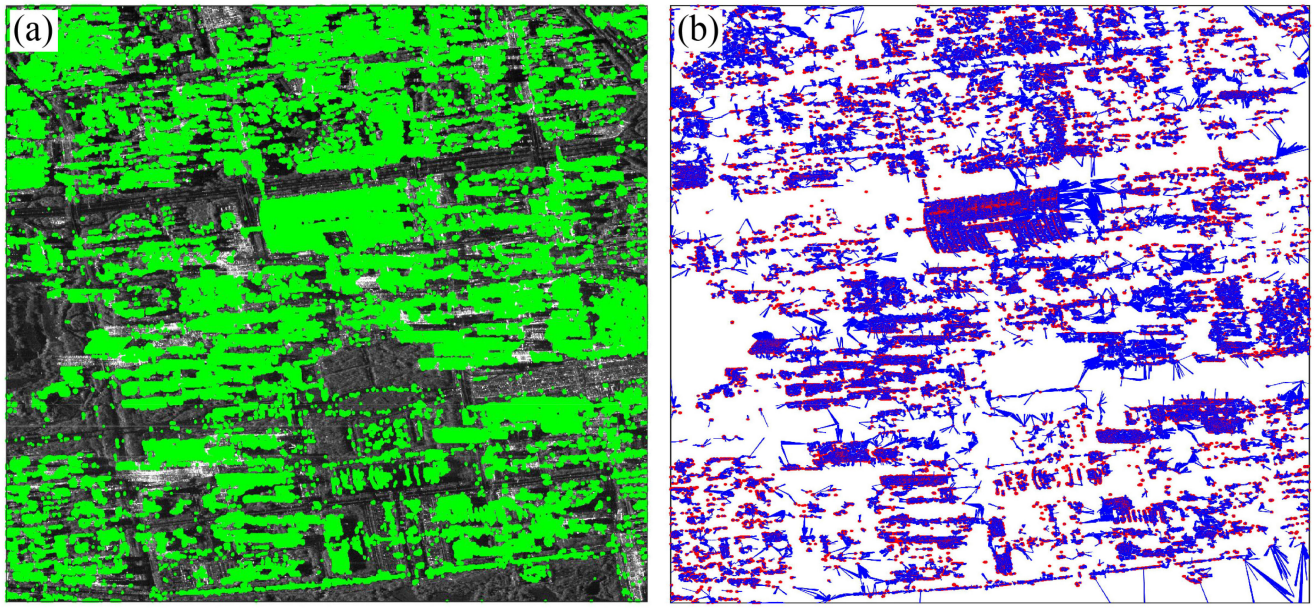

Fig. 11. (a) RPSCs selected in the second-tier network. (b) Local star networks, and the red points are the PSs detected in the first-tier network.

by direct integration in the second-tier network, as shown in Fig. 12(d)–(f). Similarly, Fig. 12(d) is the deformation velocity map in the LOS direction, ranging from –8 to 8 mm/year, Fig. 12(e) shows the height values of study area, with a range of 0–230 m, and the thermal amplitudes [see Fig. 12(f)] are mainly between 0 and 3 mm/°C. However, the second-tier network has denser measurements, thus revealing a slight settlement in individual building. Such deformation can be caused by overextraction of groundwater, soil compaction, great pressure of high-rise buildings, continuous action of ground load, and underground construction. Additional drilling data and geological maps are required for a better understanding of the causes of settlement.

D. Combination of the Results Estimated in the Two-Tier Network

We combine the most reliable PSs detected in the first-tier network and the remaining PSs detected in the second-tier network to generate an overall result. In total, 239 108 PSs were detected in the two-tier network in the whole area, yielding an improvement of 70% by compared to the PSs detected in the first-tier network [see Fig. 12(g)–(i)]. Fig. 13 presents the PS heights of the Shenzhen CITIC Building detected by the two-tier network method. Obviously, the second-tier network increases the density of the measurements in the first-tier network, thus deriving a more complete information. In general, the linear deformation of the study area is within an allowable range, except for individual building. The elastic thermal expansion effect permeates every level of the high-rise buildings, its magnitude increases with increasing height and cross-sectional area. The separation of linear deformation and thermal expansion can facilitate the discovery of possible abnormal deformations in complex deformation patterns, otherwise, thermal displacements may bias deformation velocity and height.

V. Discussions

A. Superiority of the Proposed NORM Algorithm

The comparison of different networks and estimators is listed in Table I. In the primary first-tier network, the RMS value and consumed time estimated by the WLS estimator are 1.01 rad and 935 s, respectively. After network optimization, the RMS value decreases to 0.93 rad within 722 s. Moreover, the RMS value derived from optimized first-tier network and ridge estimator is 0.82 rad, implying that the proposed NORM algorithm offers PSI a robust parameter estimation in an acceptable computation burden. The results quantitatively illustrate the importance of the reference network for PSI. Therefore, the future research may adopt the local Delaunay triangulation network with more dense and shorter arcs. Based on these networks, the ridge estimator may show a better performance in the retrieval of the absolute parameters of the PSs.

Fig. 14 presents the parameters retrieved by the two-tier networks used in [27] and in this study. By comparing the two results, it can be noted in Fig. 14(a) that the deformation velocity results derived by the two-tier network in [27] are contaminated by the existence of outliers, even a false uplift as circled by ellipse. Conversely, the proposed method is capable of generating more robust estimates due to the exploitation of the outlier detection, as shown in Fig. 14(d). Besides, compared with the results in Fig. 14(b) and (c), the proposed method has increased spatial continuity, owing to the broader distribution of the most reliable PSs in the first-tier network [see Fig. 14(e) and (f)]. Therefore, it is believed that the improved two-tier network has better performance in the study area than the traditional one. It is worth mentioning that although the proposed NORM algorithm is originally designed for urban areas, it has the potential to serve the suburb or mountainous areas where large height difference or phase decorrelation exist.

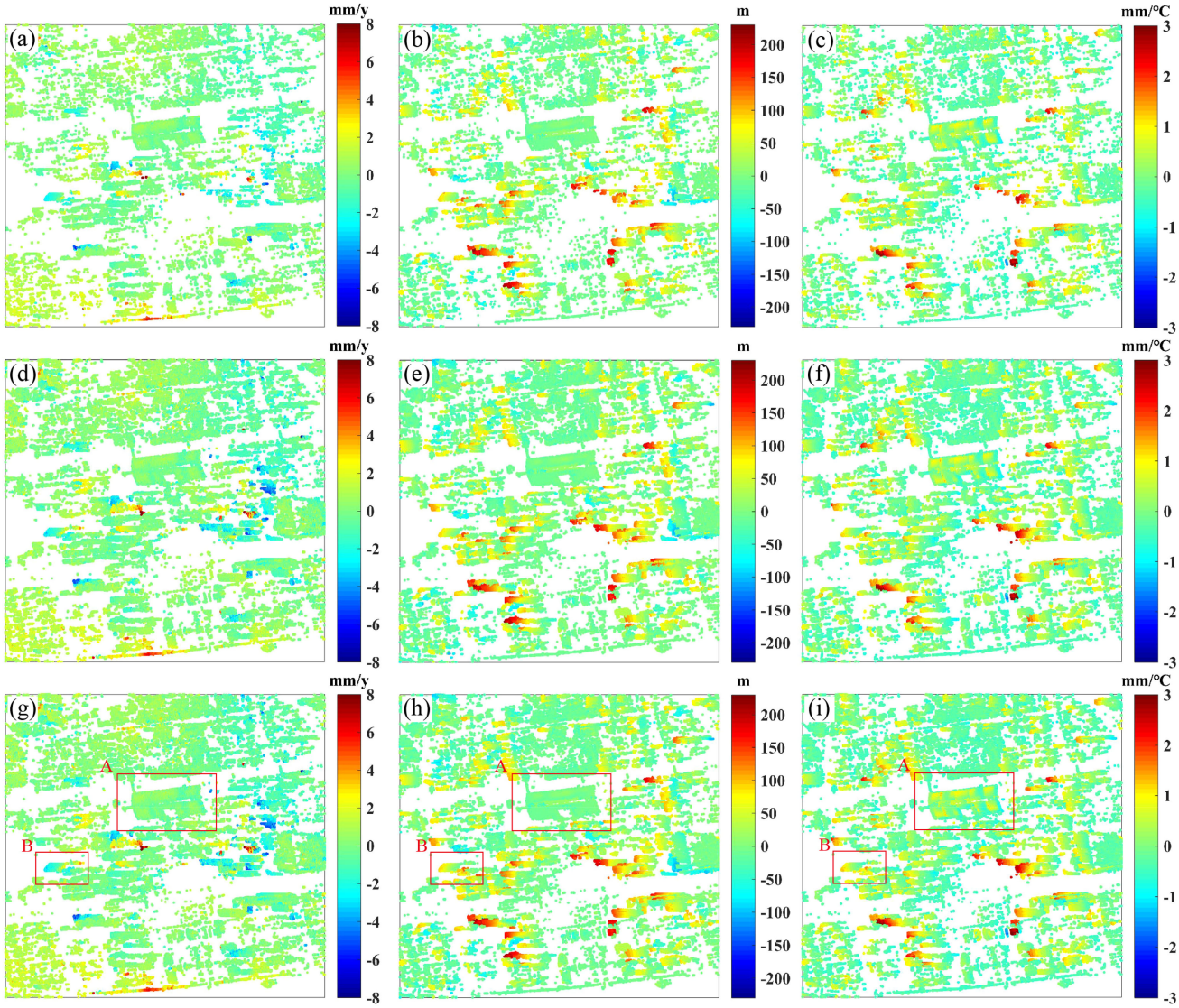

Fig. 12. (a) Deformation velocity, (b) height, and (c) thermal amplitude estimated by the first-tier network. (d) Deformation velocity, (e) height, and (f) thermal amplitude estimated by the second-tier network. (g) Deformation velocity, (h) height, and (i) thermal amplitude estimated by the two-tier network. Red rectangles represent the typical buildings.

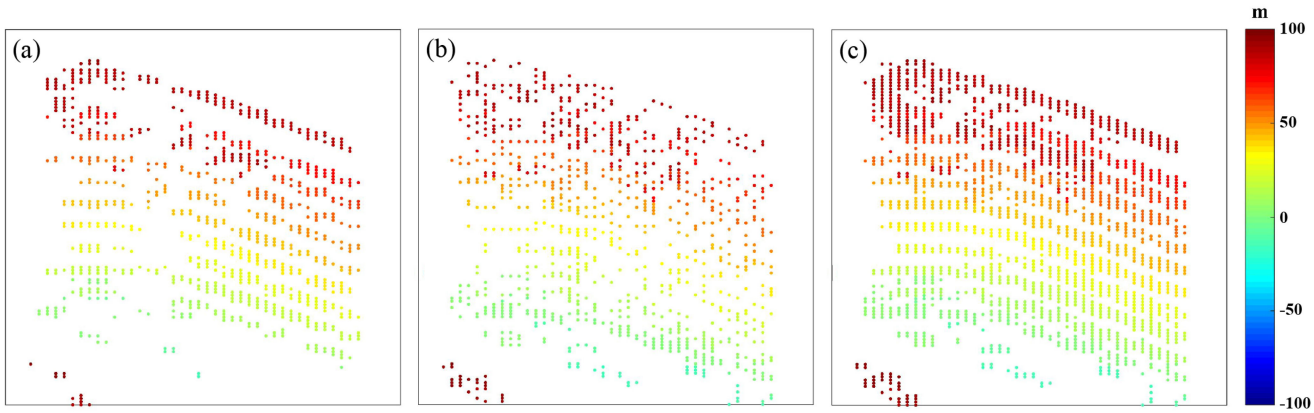

Fig. 13. PS heights of the Shenzhen CITIC Building (red rectangle of B) detected in (a) the first-tier network, (b) the second-tier network, and (c) the two-tier network.

TABLE I
COMPARISON OF DIFFERENT NETWORKS AND ESTIMATORS

	Primary first-tier network + WLS estimator	Optimized first-tier network + WLS estimator	Optimized first-tier network + Ridge estimator
RMS of phase residuals (rad)	1.01	0.93	0.82
Consumed times (s)	935	722	715

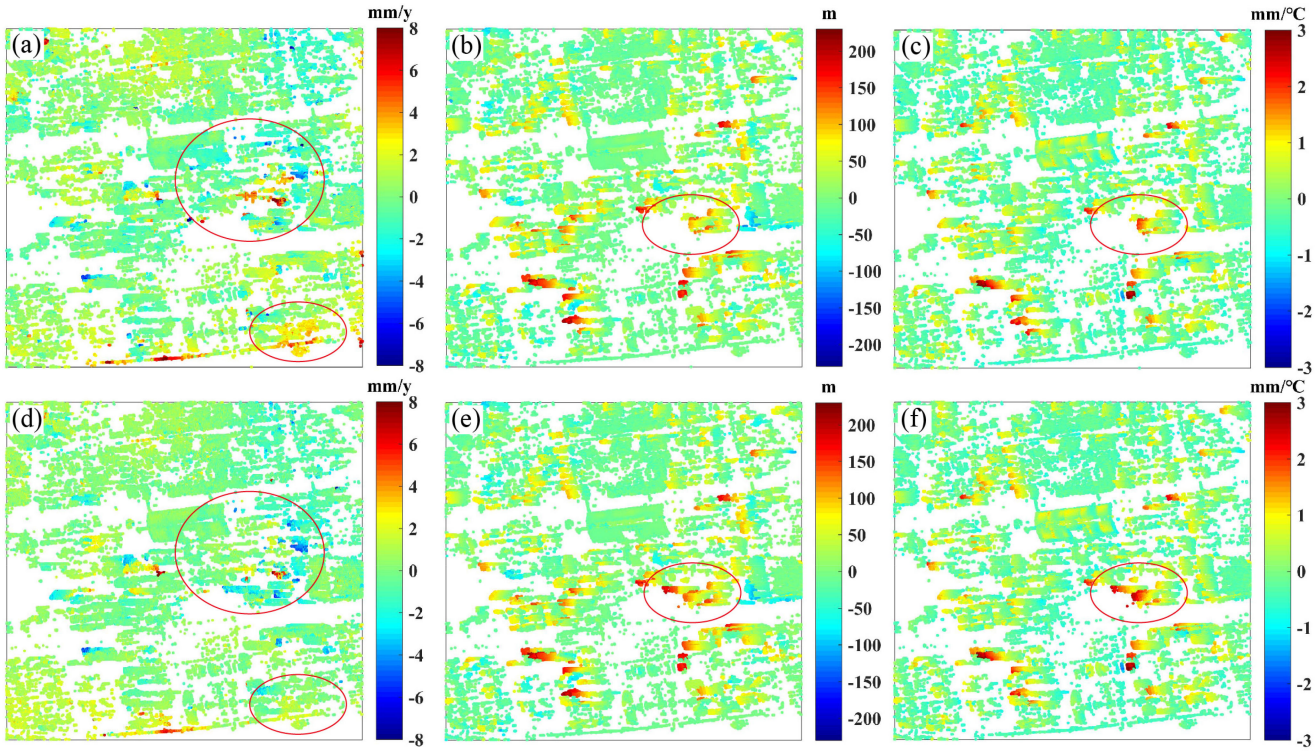

Fig. 14. First line: (a) Deformation velocity, (b) height, and (c) thermal amplitude estimated by the two-tier network in reference [27]. Second line: corresponding parameters estimated by the two-tier network improved by the proposed NORM algorithm.

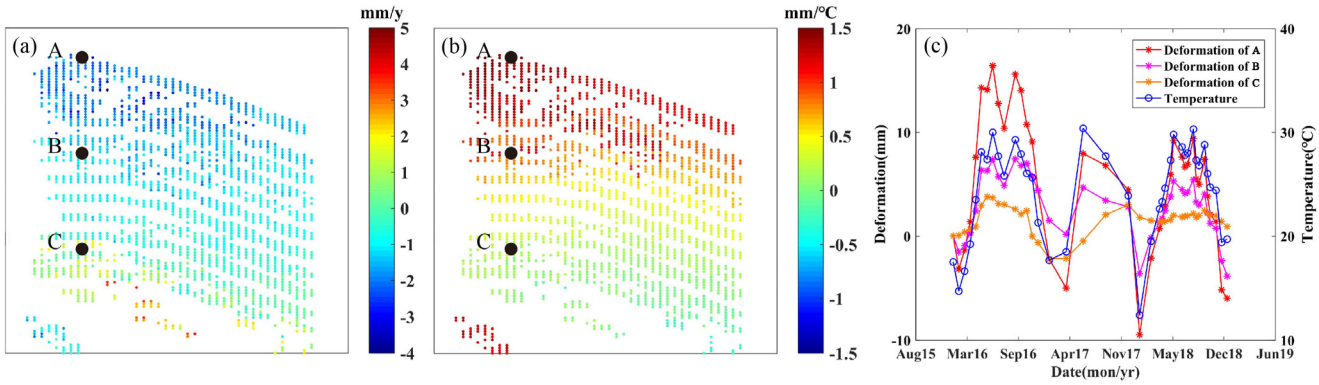

Fig. 15. (a) Deformation velocity and (b) thermal amplitude of Shenzhen CITIC Building. (c) Time-series deformation of three points (A, B, and C).

B. Analysis of Typical Buildings

Shenzhen CITIC Building and Shenzhen Convention and Exhibition Center (i.e., red rectangles of A and B) are selected to analyze the results retrieved by the proposed method. Fig. 15(a) shows the deformation velocity of the Shenzhen CITIC Building, which exhibits a height-dependent behavior in deformation velocity. Since the Shenzhen CITIC Building was newly built with respect to the observation period, the deformation phenomenon is expected, which can be triggered by concrete creep and shrinkage during concrete consolidation

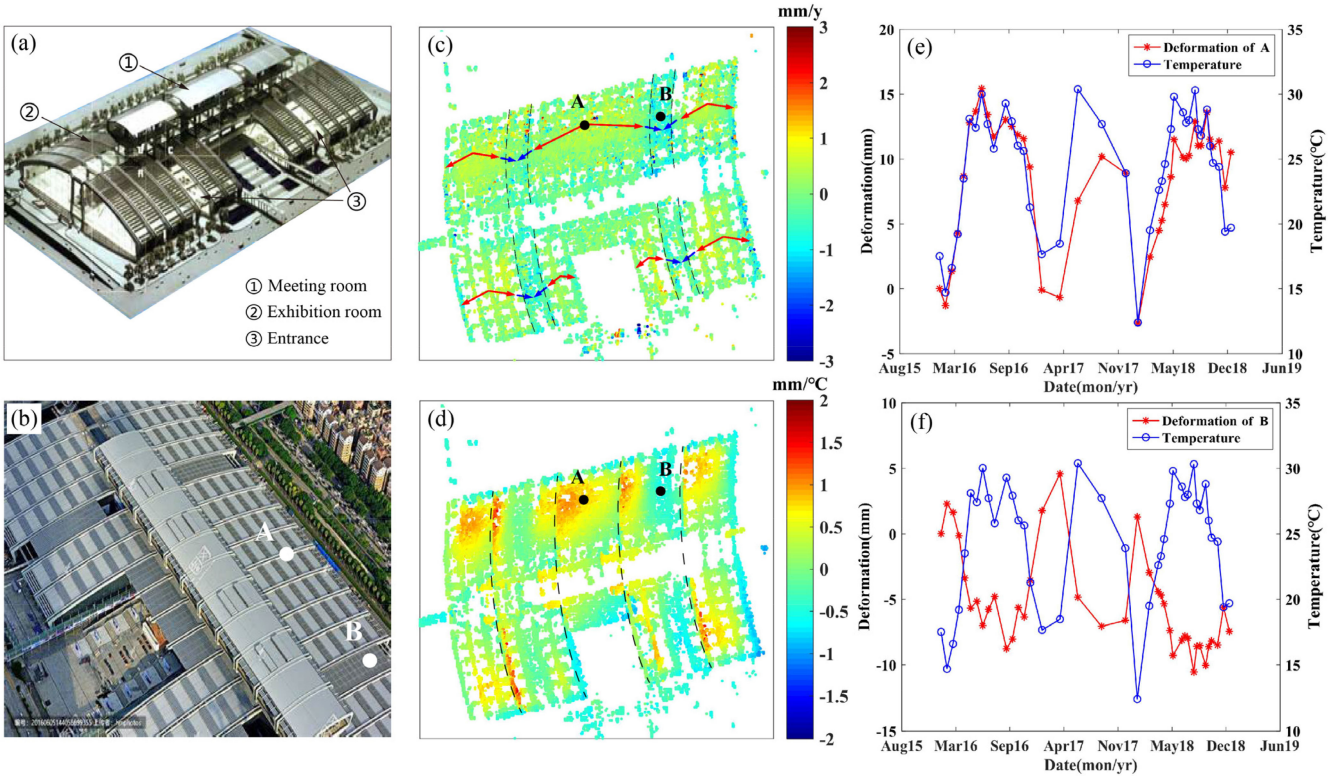

Fig. 16. (a) Skeleton frame and (b) the top view of Shenzhen Convention and Exhibition Center. (c) Deformation velocity. (d) Thermal amplitude, the dotted lines represent four expansion joints. (e) and (f) Time-series deformation of two points (A and B).

[3]. The thermal amplitude [see Fig. 15(b)] has a value that ranges approximately from 0 to 1.5 mm/°C, and displays strong and positive correlations with the height. Note that these values refer to the LOS direction. This means that a typical temperature variation between summer and winter in Shenzhen, e.g., 15 °C, induces LOS displacements of up to 20 mm in these building. The thermal expansion parameter of 1.5 mm/°C corresponds to 100 m of the building. This indicates an estimated coefficient of linear thermal expansion of 11.9×10^{-6} /°C, which is a typical value for concrete and steel structures [5]. Fig. 15(c) shows the time-series deformations of three points [A, B, and C]. It can be observed that the time-series deformation is dominated by a seasonal component relevant to local temperature, which is a typical stress phenomenon (i.e., the higher the PS, the greater the amplitude). Moreover, a decelerated trend can be found in the time-series deformation as a result of the concrete shrinkage.

Shenzhen Convention and Exhibition Center, the largest single building in Shenzhen, is composed of meeting rooms (top) and exhibition rooms (bottom), and measures approximately 540 m length × 280 m width × 60 m height. Fig. 16(a) and (b) represent the skeleton frame and the top view of Shenzhen Convention and Exhibition Center. The roof of the exhibition rooms is a double-beam steel structure with glass domes. PSs are basically detected only in steel structures since the microwave is capable of penetrating the glass. Moreover, the roof of meeting rooms presents a mirror reflection, thereby losing the SAR echo signals, as shown in Fig. 16(c) and (d).

Fig. 16(c) shows the deformation velocity of the Shenzhen Convention and Exhibition Center. Weak deformation patterns, with deformation velocities ranging from 0 to 1 mm/year, are visible in the top of the exhibition rooms. In contrast, there is an inelastic compression of –1–0 mm/year at the top of the entrances. Both expansion and compression are inelastic deformation, which will adversely affect the stability of the building. Fig. 16(d) depicts the thermal amplitude. The top of the exhibition rooms carries a maximum value of 1.5 mm/°C. The most obvious thermal displacements occur in the exhibition room at point A, the existence of expansion joints has separated its heat conduction into three parts, which can effectively prevent structural damages caused by expansion and shrinkage deformation. Similarly, an elastic compression of approximately –0.5 mm/°C is estimated at the top of the entrances. The periodic deformation of buildings caused by temperature or humidity is usually a stress deformation. Fig. 16(e) and (f) show the time-series deformation of two points [A and B]. Although their deformations are related to local temperatures, there is a strong negative correlation between their deformations. The results support that the compression at the top of the entrances is caused by the expansion of the exhibition rooms.

The estimated heights of the study area are visualized in Google Earth, as shown in Fig. 17. Here, two buildings are displayed in detail in this area. Clearly, the PSs are in good agreement with the 3-D models of the buildings in Google Earth.

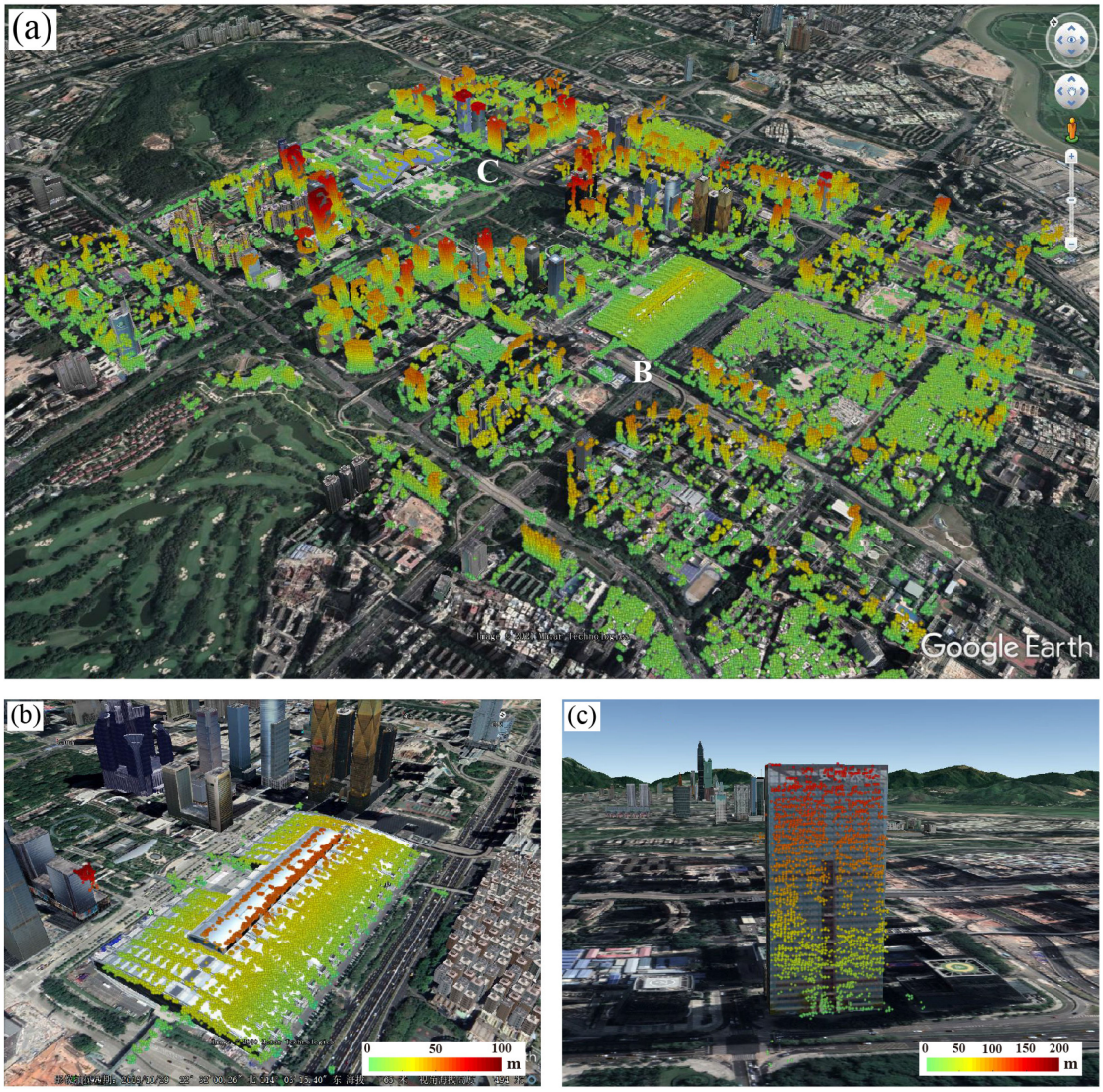

Fig. 17. (a) 3-D visualization of the PS heights in the study area. Color bar is the same as in Fig. 12(h). (b) and (c) show two buildings [B and C].

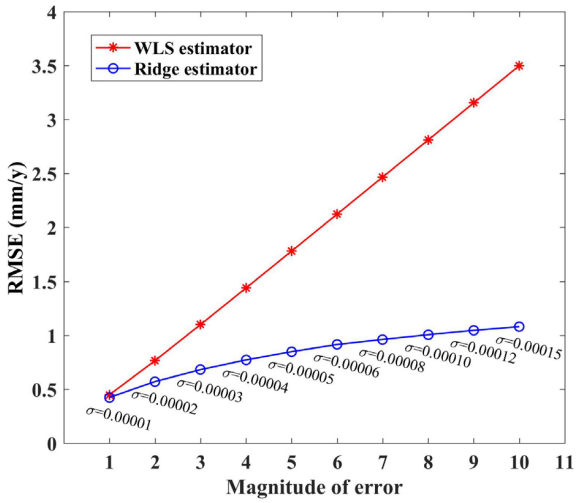

Fig. 18. RMSE of deformation velocity estimation by the WLS estimator and the ridge estimator under different magnitudes of error.

VI. Conclusion

In this article, we develop a NORM algorithm for two-tier network PSI. Such a method can increase the parameter estimation robustness and spatial continuity in single-prime mode and urban build environments. A three-parameter PSI model is employed to separate thermal expansion and deformation velocity, thus deriving elastic and inelastic displacement information. In particular, a novel two-tier network is constructed by involving outlier detection, subsets network construction, and ridge estimate in order to improve the density and accuracy of measurements. Finally, two examples of Shenzhen CITIC Building and Shenzhen Convention and Exhibition Center have been presented, which confirm that the proposed method has great potential in stress deformation monitoring of the buildings.

However, this method depends on the empirical selection of the threshold, which requires further investigation to evaluate the performance of the proposed method at different thresholds. In addition, the precision of retrieved estimations should

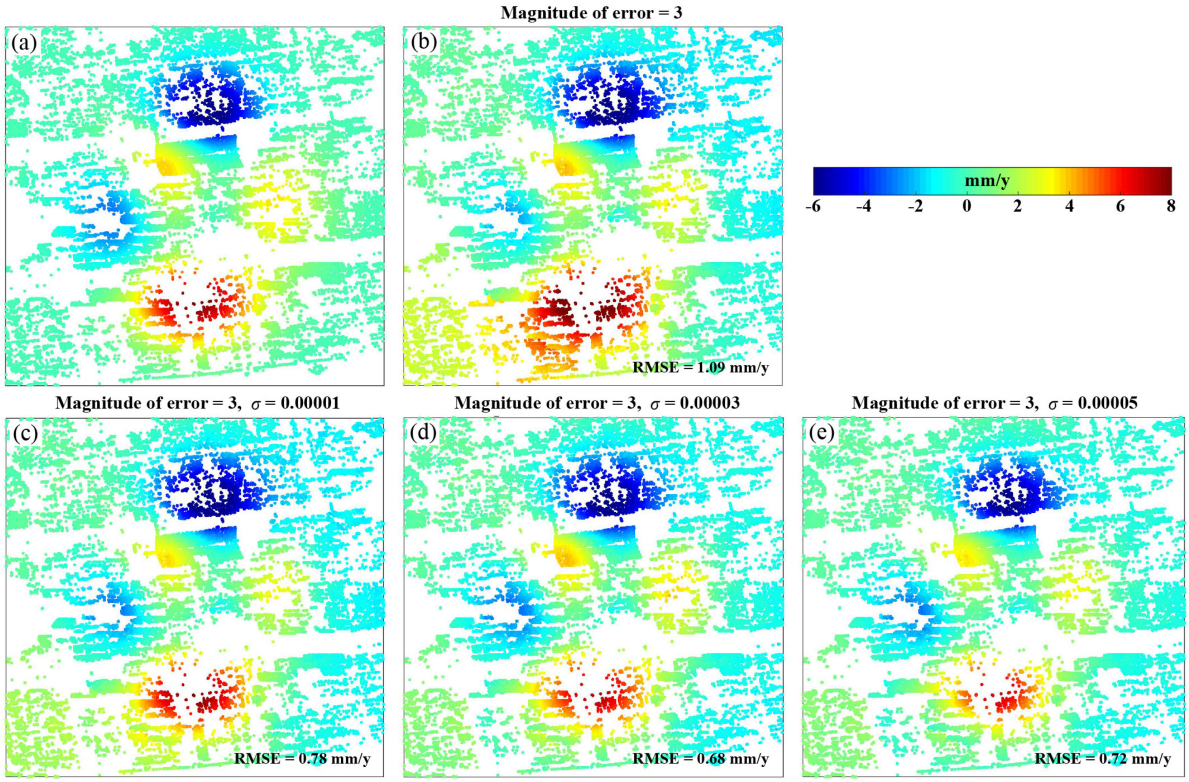

Fig. 19. (a) Simulated deformation velocity. Deformation velocity estimated by (b) the WLS estimator and (c)–(e) the ridge estimator.

be quantitatively evaluated in the future, i.e., comparing the height of the PSs with the high-precision LiDAR DEM once acquired.

Appendix

Simulated experiments are accomplished to demonstrate the performance of the WLS estimator and the ridge estimator under different magnitudes of errors, as a supplement to Fig. 10. The deformation velocity is simulated by the peaks function, as shown in Fig. 19(a). The error in Fig. 10(c) with different multiples (1–10) will be added to the simulated deformation velocity. We employ the optimized first-tier network and the PSs in real experiments to generate simulated arc measurements with errors, and then the absolute parameters on the PSs are estimated by the two estimators. Fig. 18 represents the root-mean-square error (RMSE) of the estimated deformation velocity by the WLS estimator and the ridge estimator. Obviously, the global error in the arc measurements cannot be solved by the WLS estimator, and its RMSE increases proportionally with the error. However, the ridge estimator, with a low sensitivity to global errors, can achieve better performance. The magnitude of error of 10 corresponds to an estimated RMSE of 1 mm/year. Furthermore, we found that the regulation parameter σ increases with the magnitude of error, indicating that larger errors require greater regulation.

Fig. 19(b) is the deformation velocity estimated by the WLS estimator when the magnitude of error is 3. The estimations generated by the WLS estimator have been contaminated by the global errors. Fig. 19(c)–(e) represent the deformation velocities estimated by the ridge estimator with different sigma when the magnitude of error is 3. The optimal regulation parameter is set as 3e-5 for the estimator. The good agreement shown by the simulated data confirms the soundness of the ridge estimator.

Acknowledgment

The authors would like to thank the German Aerospace Center (DLR) for providing the TerraSAR-X Data via Project MTH3683. They would also like to thank three anonymous reviewers for their constructive suggestions.

References

[1] A. Ferretti, C. Prati, and F. Rocca, "Permanent scatterers in SAR interferometry," *IEEE Trans. Geosci. Remote Sens.*, vol. 39, no. 1, pp. 8–20, Jan. 2001.

[2] S. Gernhardt and R. Bamler, "Deformation monitoring of single buildings using meter-resolution SAR data in PSI." *ISPRS J. Photogram. Remote Sens.*, vol. 73, pp. 68–79, Jul. 2012.

[3] P. Ma, H. Lin, H. Lan, and F. Chen, "Multi-dimensional SAR tomography for monitoring the deformation of newly built concrete buildings," *ISPRS J. Photogramm. Remote Sens.*, vol. 106, pp. 118–128, Aug. 2015.

[4] A. Ferretti *et al.*, "Submillimeter accuracy of InSAR time series: Experimental validation," *IEEE Trans. Geosci. Remote Sens.*, vol. 45, no. 5, pp. 1142–1153, May. 2007.

[5] O. Monserrat, M. Crosetto, M. Cuevas, and B. Crippa, "The thermal expansion component of persistent scatterer interferometry observations," *IEEE Geosci. Remote Sens. Lett.*, vol. 8, no. 5, pp. 864–868, Sep. 2011.

[6] D. Reale, G. Fornaro, and A. Pauciullo, "Extension of 4-D SAR imaging to the monitoring of thermally dilating scatterers," *IEEE Trans. Geosci. Remote Sens.*, vol. 51, no. 12, pp. 5296–5306, Dec. 2013.

[7] S. Gernhardt, X. Cong, M. Eineder, S. Hinz, and R. Bamler, "Geometrical fusion of multitrack PS point clouds," *IEEE Geosci. Remote Sens. Lett.*, vol. 9, no. 1, pp. 38–42, Jan. 2012.
[8] Y. Wang, X. Zhu, B. Zeisl, and M. Pollefeys, "Fusing meter-resolution 4-D InSAR point clouds and optical images for semantic urban infrastructure monitoring," *IEEE Trans. Geosci. Remote Sens.*, vol. 55, no. 1, pp. 14–26, Jan. 2017.
[9] X. Zhu, Y. Wang, S. Montazeri, and N. Ge, "A review of ten-year advances of multibaseline SAR interferometry using TerraSAR-X data," *Remote Sens*, vol. 10, no. 9, pp. 1374, Aug. 2018.
[10] A. Ferretti, A. Fumagalli, F. Novali, C. Prati, F. Rocca, and A. Rucci, "A new algorithm for processing interferometric data-stacks: SqueeSAR," *IEEE Trans. Geosci. Remote Sens.*, vol. 49, no. 9, pp. 3460–3470, Sep. 2011.
[11] G. Shi, H. Lin, and P. Ma, "A hybrid method for stability monitoring in low-coherence urban regions using persistent and distributed scatterers," *IEEE J. Sel. Topics Appl. Earth Observ. Remote Sens.*, vol. 11, no. 10, pp. 3811–3821, Oct. 2018.
[12] A. Hooper, P. Segall, and H. Zebker, "Persistent scatterer interferometric synthetic aperture radar for crustal deformation analysis, with application to v olcán alcedo, galápagos," *J. Geophys. Res., Solid Earth*, vol. 112, no. B7, Jul. 2007, Art. no. B07407.
[13] A. M. Guarnieri and S. Tebaldini, "On the exploitation of target statistics for SAR interferometry applications," *IEEE Trans. Geosci. Remote Sens.*, vol. 46, no. 11, pp. 3436–3443, Nov. 2008.
[14] N. Cao, H. Lee, and H. C. Jung, "A phase-decomposition-based PSInSAR processing method," *IEEE Trans. Geosci. Remote Sens.*, vol. 54, no. 2, pp. 1074–1090, Feb. 2016.
[15] G. Fornaro, S. Verde, D. Reale, and A. Pauciullo, "CAESAR: An approach based on covariance matrix decomposition to improve multibaseline–multitemporal interferometric SAR processing," *IEEE Trans. Geosci. Remote Sens.*, vol. 53, no. 4, pp. 2050–2065, Apr. 2015.
[16] S. Samiei-Esfahany, J. E. Martins, F. van Leijen, and R. F. Hanssen, "Phase estimation for distributed scatterers in InSAR stacks using integer least squares estimation," *IEEE Trans. Geosci. Remote Sens.*, vol. 54, no. 10, pp. 5671–5687, Oct. 2016.
[17] F. Heresh and A. Falk, "InSAR uncertainty due to orbital errors," *Geophys. J. Int.*, vol. 199, pp. 549–560, Jul. 2014.
[18] A. O. Kohlhase, K. L. Feigl, and D. Massonnet, "Applying differential InSAR to orbital dynamics: A new approach for estimating ERS trajectories," *J. Geodesy*, vol. 77, pp. 493–502, Mar. 2003.
[19] A. Pepe, P. Berardino, M. Bonano, L. D. Euillades, R. Lanari, and E. Sansosti, "SBAS-based satellite orbit correction for the generation of DInSAR time series: Application to RADARSAT-1 data," *IEEE Trans. Geosci. Remote Sens.*, vol. 49, no. 12, pp. 5150–5165, Dec. 2011.
[20] M. Shirzaei and T. R. Walter, "Estimating the effect of satellite orbital error using Wavelet-based robust regression applied to InSAR deformation data," *IEEE Trans. Geosci. Remote Sens.*, vol. 49, no. 11, pp. 4600–4605, Mar. 2011.
[21] B. Xu, Z. Li, Q. Wang, M. Jiang, J. Zhu, and X. Ding, "A refined strategy for removing composite errors of SAR interferogram," *IEEE Geosci. Remote Sens. Lett.*, vol. 11, no. 1, pp. 143–147, Jan. 2014.
[22] M. Costantini, S. Falco, F. Malvarosa, F. Minati, F. Trillo, and F. Vecchioli, "Persistent scatterer pair interferometry: Approach and application to COSMO-SkyMed SAR data," *IEEE J. Sel. Topics Appl. Earth Observ. Remote Sens.*, vol. 7, no. 7, pp. 2869–2879, Jul. 2014.
[23] L. Zhang, Z. Lu, X. Ding, H.-S. Jung, G. Feng, and C.-W. Lee, "Mapping ground surface deformation using temporarily coherent point SAR interferometry: Application to Los Angeles basin," *Remote Sens. Environ.*, vol. 117, pp. 429–439, Feb. 2012.
[24] A. Hooper and H. A. Zebker, "Phase unwrapping in three dimensions with application to InSAR time series," *J. Opt. Soc. Amer. A, Opt. Image Sci.*, vol. 24, no. 9, pp. 2737–2747, Aug. 2007.
[25] S. Wu, L. Zhang, X. Ding, and D. Perissin, "Pixel-wise MTInSAR estimator for integration of coherent point selection and unwrapped phase vector recovery," *IEEE Trans. Geosci. Remote Sens.*, vol. 57, no. 5, pp. 2659–2668, May 2019.
[26] H. Luo, Z. Li, Z. Dong, P. Liu, C. Wang, and J. Song, "A new baseline linear combination algorithm for generating urban digital elevation models with multitemporal InSAR observations," *IEEE Trans. Geosci. Remote Sens.*, vol. 58, no. 2, pp. 1120–1133, Feb. 2020.
[27] P. Ma and H. Lin, "Robust detection of single and double persistent scatterers in urban built environment," *IEEE Trans. Geosci. Remote Sens.*, vol. 54, no. 4, pp. 2124–2139, Nov. 2015.
[28] X. Zhu, Z. Dong, A. Yu, M. Wu, D. Li, and Y. Zhang, "New approaches for robust and efficient detection of persistent scatterers in SAR tomography," *Remote Sens.*, vol. 11, no. 3, Feb. 2019, Art. no. 356.
[29] P. Berardino, G. Fornaro, R. Lanari, and E. Sansosti, "A new algorithm for surface deformation monitoring based on small baseline differential SAR interferograms," *IEEE Trans. Geosci. Remote Sens.*, vol. 40, no. 11, pp. 2375–2383, Nov. 2002.
[30] B. M. Kampes, *Radar Interferometry: Persistent Scatterer Technique.* Dordrecht, The Netherlands: Springer, 2006.
[31] H. Liang *et al.*, "Suppression of coherence matrix bias for phase linking and ambiguity detection in MTInSAR," *IEEE Trans. Geosci. Remote Sens.*, vol. 59, no. 2, pp. 1263–1274, Feb. 2021.
[32] P. C. Hansen and D. P. O'Leary, "The use of the l-curve in the regularization of discrete ill-posed problems," *SIAM J. Sci. Comput.*, vol. 14, no. 6, pp. 1487–1503, Nov. 1993.
[33] W. Wu, H. Cui, J. Hu, and L. Yao, "Detection and 3D visualization of deformations for high-rise buildings in Shenzhen, China from high-resolution TerraSAR-X datasets," *Appl. Sci.*, vol. 9, no. 18, Sep. 2019, Art. no. 3818.
[34] P. Misra, R. Avtar, and W. Takeuchi, "Comparison of digital building height models extracted from AW3D, TanDEM-X, ASTER, and SRTM digital surface models over Yangon city," *Remote Sens.*, vol. 10, no. 12, Dec. 2018, Art. no. 2008.
[35] J. Hu *et al.*, "Estimating three-dimensional coseismic deformations with the SM-VCE method based on heterogeneous SAR observations: Selection of homogeneous points and analysis of observation combinations," *Remote Sens. Environ.*, vol. 255, Mar. 2021, Art. no. 112298.

Wenqing Wu received the B.S. degree from Hunan University of Science and Technology, Xiangtan, China, in 2017, and the M.S. degree in 2020 from the School of Geosciences and Info-Physics, Central South University, Changsha, China, where he is currently working toward the Ph.D. degree in geomatics.

His research interests include signal processing and analysis for high-resolution SAR interferometry and multisource fusion algorithms of synthetic aperture radar.

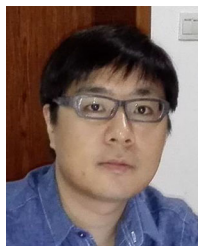

Jun Hu (Member, IEEE) received the M.Eng. and Ph.D. degrees in geodesy and surveying engineering from Central South University, Changsha, China, in 2008 and 2013, respectively.

From 2013 to 2014, he was a Postdoctoral Fellow with the Department of Land Surveying and Geo-Informatics, The Hong Kong Polytechnic University, Hong Kong. He is currently a Full Professor with the Department of Geomatics and Remote Sensing, School of Geosciences and Info-Physics, Central South University. He has authored more than 60 papers in international peer-reviewed journals. His research interests include mapping multidimensional and high-precision deformations under complicated environment and its applications in geophysical fields.

Zhigui Du is currently the Vice President of SPACETY, Changsha, China. He was the Director of Space System Department of AOE CAS. He has been engaged in the overall design of space mission, space system and mechanical and electrical engineering for a long time. He has rich experience in aerospace engineering and mechanical engineering, and has in-depth research on space mission planning, spacecraft design, satellite AIT, etc.

Jingxin Hou received the bachelor's degree in surveying and mapping engineering from Central South University, Changsha, China, in 2015. He is currently working toward the doctoral degree in the Institute of Radar Remote Sensing & Imaging Geodesy (RRSIG), Central South University, Changsha, China.

His research interests include algorithm developments for multitemporal InSAR technique and monitoring deformations of infrastructures in large-scale areas.

Wanji Zheng was born in Haikou, China, in 1992. He received the B.S. and M.E. degrees in geomatics, in 2015 and 2018, respectively, from Central South University, Changsha China, where he is currently working toward the Ph.D. degree in geodesy and survey engineering.

His research interests include retrieving 3-D surface displacement with synthetic aperture radar technique and its application in landslide monitoring.

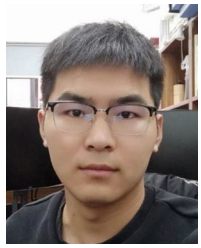

Jihong Liu received the bachelor's degree in 2017 from the School of Geosciences and Info-Physics, Central South University, Changsha, China, where he is currently working toward the Ph.D. degree in geodesy and surveying engineering.

His current research interests include InSAR and its applications on time-series deformation and 3-D surface deformation mapping.